

Statistical and Deterministic RCS Characterization for ISAC Channel Modeling

Ali Waqar Azim, Ahmad Bazzi, Roberto Bomfin, Nikolaos Giakoumidis, Theodore S. Rappaport, Marwa Chafii

Abstract—In this study, we perform a statistical analysis of the radar cross section (RCS) for various test targets in an indoor factory at 25–28 GHz, with the goal of formulating parameters that may be used for target identification and other sensing applications for future wireless systems. The analysis is conducted based on measurements in monostatic and bistatic configurations for bistatic angles of 20°, 40°, and 60°, which are functions of transmitter-receiver (T-R) and target positions, via accurate 3dB beamwidth of 10° in both azimuth and elevation planes. The test targets include unmanned aerial vehicles, an autonomous mobile robot, and a robotic arm. We utilize parametric statistical distributions to fit the measured RCS data. The analysis reveals that the *lognormal* and *gamma* distributions are effective in modeling the RCS of the test targets over different reflecting points of the target itself, i.e. when target is in motion. Additionally, we provide a framework for evaluating the deterministic bistatic RCS of a rectangular sheet of laminated wood, due to its widespread use in indoor hotspot environments. Novel deterministic and statistical RCS models are evaluated, incorporating dependencies on the bistatic angle, T-R distance (2m -10m) and the target. The results demonstrate that some proposed RCS models accurately fit the measured data, highlighting their applicability in bistatic configurations.

Index Terms—radar cross section, bistatic, integrated sensing and communications, indoor factory, indoor hotspot.

I. INTRODUCTION

Integrated sensing and communications (ISAC) combines wireless communications and radar sensing to efficiently utilize scarce radio resources and shared hardware for dual purposes, with two primary configurations: monostatic and bistatic [1]. For sensing, the target’s radar cross section (RCS) characterization is an important aspect of ISAC channel modeling. The RCS is an intrinsic property of the target and is independent of the radar system, determined by factors such as the geometric structure, the material composition, and the operating frequency, among others [2], [3], [4]. The RCS can be modeled using deterministic or statistical approaches [2]. Deterministic RCS modeling utilizes numerical and geometric techniques to compute the RCS with precision. In addition, deterministic RCS modeling considers various elements, such as the structural characteristics of the test object and the operating frequency. In contrast, statistical RCS modeling

This work is supported in part by the NYUAD Center for Artificial Intelligence and Robotics, funded by Tamkeen under the Research Institute Award CG010.

Ali Waqar Azim, Ahmad Bazzi, Roberto Bomfin, and Marwa Chafii are with the Engineering Division, New York University Abu Dhabi (NYUAD), 129188, UAE (email: ali.waqar.azim,ahmad.bazzi,roberto.bomfin,marwa.chafii@nyu.edu). Ahmad Bazzi, Theodore S. Rappaport and Marwa Chafii are with NYU WIRELESS, NYU Tandon School of Engineering, Brooklyn, 11201, NY, USA (email: tsr@nyu.edu). Nikolaos Giakoumidis is KINESIS Lab, Core Technology Platforms, NYUAD, 129188, UAE and with Intelligent Systems Lab, Cultural Technology and Communication, University of the Aegean, 811 00 Mitilini, Greece (email: giakoumidis@nyu.edu).

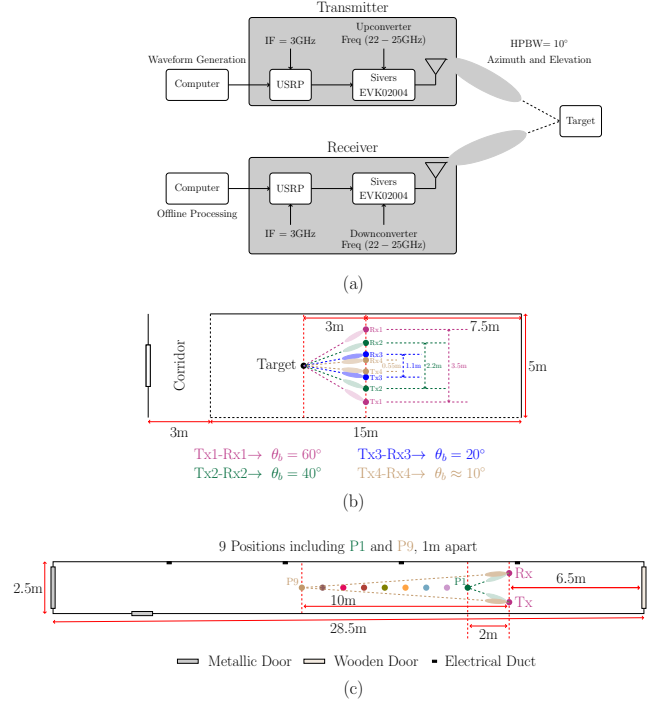


Fig. 1: (a) Testbed for the RCS measurement, (b) the layout of the measurement environment for statistical RCS analysis, (c) the layout of the measurement environment for deterministic RCS analysis.

represents the RCS as a random variable characterized by a specific probability density function (PDF) [5].

A. Measurement Setup & Considerations

Our measurement testbed is described in Fig. 1(a), which provides a block diagram representation of the bistatic system model used for RCS measurements. Our testbed contains a signal generation, upconversion, transmission, and a symmetrical reception process. The system employs a universal software radio peripheral (USRP) for waveform generation and digitization, with the Siivers EVK02004 handling radio-frequency (RF) upconversion and downconversion. The measurement operates over a frequency range of 25–28 GHz, with an intermediate frequency (IF) of 3 GHz. The transmitter (Tx) and receiver (Rx) antennas are aligned to ensure proper signal reflection and capture. The half-power beamwidth is 10° in elevation and azimuth. The Tx and Rx radio-frequency integrated circuits (RFICs) are interfaced with B205mini USRPs, having a bandwidth of 20 MHz, each. The Tx employs a known Zadoff-Chu (ZC) sequence of length 128 as the transmitted signal, generated using MATLAB. At the Rx, the signal is processed to extract the channel impulse response (CIR). In order to change the output frequency of the RFIC, the upconverter and downconverter frequencies are changed in steps of 1GHz.

Subsequently, the radio-frequency integrated circuits (RFICs) at both Tx and Rx are calibrated for the updated frequencies.

Figs. 1(b) and 1(c) provide a top-view representation of the measurement setups, including antenna orientations, distances, and bistatic angles. Fig. 1(b) illustrates the statistical RCS characterization setup, showing four distinct Tx-Rx pairs positioned at different bistatic angles with the boresight of the antenna tilted towards the target. Fig. 1(c) depicts the deterministic RCS setup in a corridor, where the target moves along predefined positions (P1 to P9), altering the bistatic angle. In both setups, the Tx and Rx are carefully aligned to ensure accurate signal reflection and capture over the specified distances. Our indoor factory (InF) environment is the KINESIS Lab, Core Technology Platforms, located two floors below the Arts Center at the New York University (NYU) Abu Dhabi campus, in Saadiyat Island, Abu Dhabi, the United Arab Emirates. The InF layout is 5 m in width, 15 m in length and 8.5 m in height, which is sufficient to fly small and medium sized unmanned aerial vehicles (UAVs). The indoor hotspot (InH) environment is an indoor corridor nearby the KINESIS lab, which is 2.5 m in width, 28.5 m in length and 2.5 m in height. The total amount of data collected throughout our entire campaign is 3.544 gigabytes. For the statistical case, *the RCS is measured during motion of the target, which can capture a statistical representation of the target in question.*

Our statistical RCS analysis includes two UAVs that differ in size and material composition, and are observed in distances ranging from 3m to 3.5m from the Tx/Rx. For robotic systems, we examine an autonomous mobile robot (AMR) and a robotic arm (RA). For UAVs, the RCS is measured during flight and rotational motion, while for the AMR and RA, the data is collected as they emulate tasks typically performed in an InF setting. All measurements were conducted in line-of-sight (LoS) conditions with horizontal (H) polarization for both the Tx and Rx. Parametric distributions are employed to model the measured RCS data for statistical analysis, via goodness-of-fit (GoF) metrics, which are the Kolmogorov-Smirnov (KS) statistic and the mean squared error (MSE), which provide quantitative measures of the accuracy of the fit. For sensitivity, the analog-to-digital converter (ADC) of the USRP has a resolution of 12 bits, while the ADC of the RFIC has a resolution of 10 bits.

In addition to statistical modeling of RCS for common factory objects, we also sought to determine the near-field (NF) RCS of common objects found in factories, such as a rectangular sheet of laminated wood in an InH environment for operating frequencies ranging from 25 GHz to 28 GHz, via a deterministic RCS framework. Laminated wood is widely used in modern offices for everything from desktops and meeting tables to cabinets and wall cladding, thanks to its durability, range of aesthetic finishes, and easy maintenance. Path loss (PL) measurements are collected across various bistatic angles to evaluate the RCS deterministically. We propose multiple RCS models that depend on the bistatic angle and the distance between the Tx/Rx and the target's center. Our deterministic model is a modified version of the floating intercept (FI) model, in a sense that it accounts twice for double PL and introduces an RCS term (see Section IV-B for more details).

After fitting onto the modified FI model, we assess different NF RCS expressions to find the best NF RCS in terms of the lowest mean fitting error (MFE). All measurements are conducted under LoS conditions, with H-polarization for Tx and Rx. In addition to fitting the RCS, other parameters such as the PL exponent, intercept, and shadowing factor are also estimated. The fitting results indicate a strong dependence of the RCS on the bistatic angle.

B. Standardization Progress and RCS

While RCS was considered decades ago in the early days of the cellphone industry for channel modeling, the sparsity of large buildings in macrocells made the approach much less valuable than today's applications, where the excellent temporal resolution (in the order of nanoseconds) and antenna directionality offered by the small wavelengths of millimeter wave and terahertz frequencies makes the use of RCS viable for ISAC applications [6], [7]. Using the RCS method to identify objects is particularly effective when the backscatter echo power from the target exhibits fluctuations due to variations in its scattering properties or changes in its cross-sectional areas [7]. The measured RCS data may then be fitted to parametric statistical distributions, for lookup tables and future use in learning and optimization as more measurements are collected for the identified object(s). The distribution(s) demonstrating robust GoF metrics with the measured data are selected to represent the target's RCS. Importantly, the 3rd Generation Partnership Project (3GPP) endorses statistical RCS modeling for ISAC channel modeling [8], highlighting its significance in capturing dynamic and fluctuating target behaviors, besides channel modeling for the upper mid-band as part of 6G [9].

II. STATISTICAL RCS CHARACTERIZATION OF INDOOR FACTORY TARGETS

In this section, we provide the statistical RCS characterization of InF targets.

A. Indoor Factory Targets

The InF environment, shown in Fig. 1(b), is the KINESIS Lab, Core Technology Platforms, which is 2 floors below the Arts Center at NYU Abu Dhabi campus. The InF layout is 5 m in width, 15 m in length and 8.5 m in height. In our measurements, the targets we consider are commonly found in InF environments, which include (i) two types of UAVs; (ii) an RA; and (iii) an AMR, referred to as the quadruped robot (QR). The specifications of the targets are given in Table I. The unfolded configurations of the UAVs are presented in Fig. 2(a) and (b). Fig. 2(a) illustrates the Mavic 2 Pro, while Fig. 2(b) displays the Matrice 300 RTK. The Mavic 2 Pro and Matrice 300 RTK UAVs' respective folded and unfolded dimensions are detailed in Table I. In addition to the UAV size, different orientations of the UAVs play a critical role in characterizing the RCS dependency. Therefore, measurements were conducted with the UAVs in flight, rotating steadily above the observation point, which ensures capturing backscatter reflections at Rx from all possible UAV orientations. The vertical distance between the ground and the bottom of the

TABLE I: Specifications of Equipment Used in Measurements

Equipment	Dimensions	Mass	Materials
DJI Mavic 2 Pro	Folded: $214 \times 91 \times 84$ mm Unfolded: $322 \times 242 \times 84$ mm	907g	Magnesium alloy, reinforced plastic, carbon fiber, glass, silicon components
DJI Matrice 300 RTK	Folded: $430 \times 420 \times 430$ mm Unfolded: $810 \times 670 \times 430$ mm	3.6-6.3kg	Carbon fiber-reinforced plastic, aluminum, plastic
Robotic Arm (KUKA LBR iiwa 14 R820)	Reach: 820 mm Height: 1640 mm (with arm)	≈ 30 kg	Aluminum, titanium, steel, plastic, polymer composites
Quadruped Robot (Boston Dynamics Spot)	Length: 1100 mm; Width: 500 mm; Height: 610 mm (walking without arm)	≈ 32.7 kg	Aluminum, titanium, carbon fiber composites, polymer



(a) Mavic 2 Pro



(b) Matrice 300 RTK

Fig. 2: UAV test targets used in the study.



(a) Robotic Arm



(b) Quadruped Robot

Fig. 3: InF equipment used in the study: (a) RA, (b) QR.

UAVs is also different due to their dimensional differences. For Mavic 2 Pro, this distance was approximately 0.9m, while for Matrice 300 RTK, it was approximately 0.6m. Another factor influencing the RCS is the placement of the lithium-ion battery. For the Matrice 300 RTK, the battery is mounted on one side, whereas for the Mavic 2 Pro, the battery is positioned on top of the UAV. The design difference of both drones is expected to result in stronger specular reflections from the Matrice 300 RTK, compared to the Mavic 2 Pro. Note that UAVs were flying over the observation point during the measurement process. The *Observation point* is located 3m away from the center of the line segment connecting Tx and Rx. The Tx and Rx bore-sight beams also converge at that observation point.

The second target under consideration is the RA, as shown in Fig. 3a. The reach and height specifications of the RA are detailed in Table I. Measurements were conducted with RA positioned at the observation point and continuously moving, utilizing its seven joints to perform various tasks characteristic of its operation in an InF setting, including pick-and-place operations, etc. The RA's maximum achievable height is 1640 mm. However, it can be significantly reduced during specific motions, such as those that simulate pick-and-place tasks, thereby decreasing the reflective surface area.

The third target is the QR, depicted in Fig. 3b. The

dimensions of the QR are provided in Table I. RCS measurements were conducted while the QR was in motion around the observation point, with two distinct types of movements analyzed: (i) lateral motion along the observation point and (ii) longitudinal motion towards and away from the observation point. The lateral and longitudinal motions replicate the typical operational patterns of QRs in InF. The lateral motion captures the robot's side profile, while the longitudinal motion focuses on the front/back profile, providing RCS measurements across different orientations. A non-conducting object of 20 cm height was placed at the observation point. The QR moved vertically up and down the non-conducting object.

B. Experimental Setup and RCS Evaluation Methodology

In this work, we employ monostatic and different bistatic configurations with bistatic angles, θ_b of 20° , 40° , 60° . For the monostatic configuration, $\theta_b = 0$, however, it is impossible to have $\theta_b = 0$ in practice. Therefore, we employ a quasi-monostatic configuration in which the Tx and Rx are separated by 55 cm, leading to $\theta_b \approx 10^\circ$. An illustration of the experimental setup is shown in Fig. 4. The distance between the Tx and the Rx is given as $d_{Tx,Rx}$, the distance between the Tx and the target is $d_{Tx,tar}$, and the distance between the Rx and the target is $d_{Rx,tar}$. Moreover, the distances, $d_{Tx,tar}$ and $d_{Rx,tar}$ are always the same. The actual measurements are carried out in an InF environment as shown in Fig. 5. The distances $d_{Tx,Rx}$, $d_{Tx,tar}$, and $d_{Rx,tar}$ are also illustrated in Fig. 5. The Tx and the Rx are placed in the middle of the InF environment ($15 \times 5 \times 8.5$ m). The environment includes the dense clutter characteristic of typical InF scenarios, ensuring realistic propagation conditions. Moreover, the height of the Tx and Rx is 1 m from the ground. The operating frequencies that we consider are 25 – 28 GHz. Moreover, H-polarizations are considered for both Tx and the Rx.

The Tx and Rx used in these measurements are Siivers EVK02004 RFICs, featuring a half-power beamwidth of 10° in both azimuth and elevation planes. Each RFIC incorporates a 16-element (4×4) antenna array. The Tx and Rx RFICs are interfaced with B205mini USRPs, having a bandwidth of 20 MHz. The USRPs operate at an IF of 3 GHz. The Tx employs a known ZC sequence of length 128 as the transmitted signal, generated using MATLAB. ZC sequences are specifically chosen due to their constant amplitude and optimal correlation properties. At the Rx, the signal is processed to extract the CIR. The CIR encapsulates information regarding the propagation environment, including the presence or absence of a target, by capturing reflections and scattering characteristics within the channel.

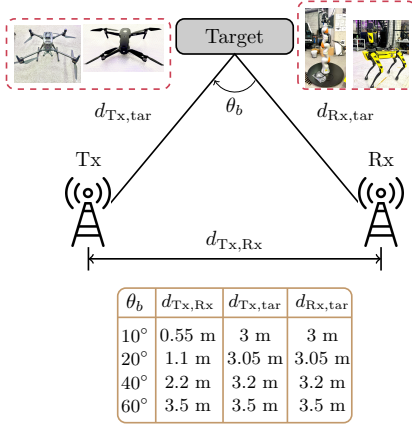


Fig. 4: An illustration of the measurement setup configuration.

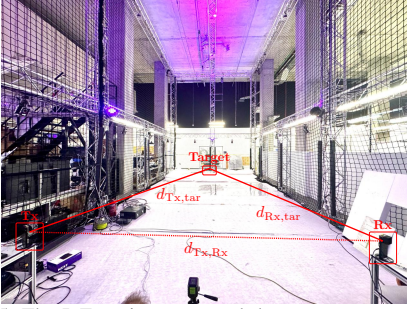


Fig. 5: The InF environment and the measurement setup.

During the preliminary stage of the measurement process, the CIRs are acquired for both monostatic and bistatic configurations for all θ_b and operating frequencies in the absence of the target. Reference CIRs, termed as background CIRs, and denoted as $h_{\text{back}}(n)$, comprehensively encapsulates the intrinsic contributions of environmental clutter and static scatterers within the measurement domain for different θ_b and frequencies. $h_{\text{back}}(n)$ serves as a benchmark, facilitating the precise discrimination of target-induced reflections from ambient propagation artifacts in subsequent analysis.

The CIRs, $h(n)$ are subsequently estimated in the presence of the target across the configurations above and operating frequencies. The measurements capture alterations in the propagation environment introduced by the target, $h(n)$, comprising the contributions by $h_{\text{back}}(n)$ and the target-specific components denoted as $h_{\text{tar}}(n)$. Firstly, the total power is evaluated as $P_{\text{tot}} = \sum_n |h(n)|^2$. P_{tot} contains the power contribution from both the target and the background, i.e., $P_{\text{tot}} = P_{\text{tar}} + P_{\text{back}} + P_{\text{noise}}$, where P_{noise} is the noise power. Next, we evaluate the P_{back} as $P_{\text{back}} = \sum_n |h_{\text{back}}(n)|^2$. The target power is then evaluated as $P_{\text{tar}} = P_{\text{tot}} - P_{\text{back}} - P_{\text{noise}}$. P_{tar} represents the power contribution exclusively due to the target-induced scattering and reflections. P_{tar} is obtained for all targets in both monostatic and bistatic configurations for all θ_b and operating frequencies, constructing a comprehensive measurement dataset of target-specific power responses across the measurement configuration and frequency space. P_{tar} contains an accurate representation of the target's RCS. Considering $d_{Tx,tar} = d_{Rx,tar} = d$, P_{tar} can be expressed as:

$$P_{\text{tar}} = \frac{P_t G_{Tx} G_{Rx} \sigma \lambda^2 L}{(4\pi)^3 d^4}, \quad (1)$$

where P_t is the transmit power, G_{Tx} is the Tx gain, G_{Rx} is the Rx gain, λ is the wavelength, σ is the RCS in m^2 , L are unknown system losses. Also note that, apart from λ , $d_{Tx,tar}$, and $d_{Rx,tar}$, all other parameters in (1) are system-specific. Consequently, a calibration step is crucial to accurately determine these unknown system parameters before reliable RCS can be obtained. The calibration process consists of placing the Rx at the target position, where the received power follows the free space PL as $P_{Rx} = \frac{P_t G_{Tx} G_{Rx} \lambda^2 L}{(4\pi)^2 d^2}$, which is computed through extensive measurements, then a system factor quantity is computed as $K(\lambda, d) = \frac{P_{Rx}}{4\pi d^2}$. The factor $4\pi d^2$ is to match the powers of the single and double PLs. Finally, during measurement phase, the RCS of a test target is obtained as $\sigma = K^{-1}(\lambda, d) P_{\text{tar}}$.

C. Parametric Distributions and Goodness-of-Fit Tests

To model and analyze the RCS, various parametric distributions are used to fit the measured data, with each distribution tailored to capture specific statistical characteristics of the measured data. Distributions such as normal, lognormal, Rayleigh, gamma, exponential, and Weibull are systematically considered, using their distinct features to see how these distributions capture the effects of the measured data. The normal distribution is suitable for datasets exhibiting symmetric behavior around the mean. However, for positively skewed data, which is the case with the measured RCS, the lognormal and Weibull distributions are more effective, as they can capture the asymmetry and heavy-tail behaviors often associated with specular and diffused reflections reflecting from the test targets. The gamma distribution is particularly well suited to modeling a wide range of skewness. Therefore, it is especially adept at characterizing the measured RCS data influenced by the mixture of strong and weak reflections. The exponential distribution effectively captures the positively skewed nature of such data, assuming that smaller RCS values occur more frequently while larger values are exponentially less likely, which can capture scenarios where the channel is dominated by LoS reflections. Parametric distributions aligned with the measured RCS data enable the extraction of statistical parameters that not only characterize the data but also reveal nuanced reflective properties of the test targets.

The normal distribution is defined by the mean, μ , and the standard deviation, $\sigma > 0$. The lognormal distribution uses the mean, μ and the standard deviation, $\sigma \geq 0$ of the natural logarithm of the variable. The gamma distribution has a shape parameter, $A > 0$, and a scale parameter $B > 0$, controlling the form and spread. The Weibull distribution is also defined by the shape $B > 0$ and scale $A > 0$. The Rayleigh distribution uses a scale parameter $B > 0$ for spread, and the exponential distribution is based on the rate parameter $\lambda > 0$, which governs the decay rate.

The GoF of the parametric distributions is evaluated using the KS statistic and MSE, which offer further insights into the accuracy of fit between the parametric distribution we consider and the measured RCS data. Moreover, it allows us to determine which distribution can be used to model the RCS for ISAC channel modeling.

The KS statistic measures the maximum absolute deviation between the empirical cumulative distribution function (CDF), $F(x)$, and the theoretical CDF of the fitted model, $F_{\text{fitted}}(x)$, which is sensitive to differences in the general shape of the distribution and shows regions where the model cannot mimic important features of the empirical data. A smaller KS statistic indicates a closer fit between the parametric distribution and the measured data. In contrast, a larger KS statistic value suggests a poor fit. The KS statistic is expressed as

$$\text{KS Statistic} = \max |F(x) - F_{\text{fitted}}(x)|. \quad (2)$$

The MSE evaluates the average squared difference between the empirical CDF and the fitted CDF across all data points. Unlike the KS statistic, which focuses on localized mismatches, MSE provides a broader GoF measure by capturing cumulative discrepancies between the theoretical fitted model and the measured data. Smaller MSE values indicate a closer overall agreement between the empirical and theoretical models, while higher values reflect systematic biases or poor representation of the data's statistical behavior. MSE is mathematically defined as:

$$\text{MSE} = \frac{1}{N} \sum_{i=1}^N (F(x_i) - F_{\text{fitted}}(x_i))^2, \quad (3)$$

where N is the total number of data points.

These metrics help identify the distributions that best capture the statistical characteristics of the measured RCS data, facilitating precise RCS modeling of different test targets.

III. RCS FITTING TO PARAMETRIC DISTRIBUTIONS

This subsection presents the fitting of parametric distributions to the measured RCS data. The analysis involves fitting PDFs and CDFs of the parametric distributions to the measured RCS data. The theoretical distributions' statistical parameters are optimized to fit the measured RCS data best. Due to space constraints, we illustrate the PDFs and CDFs of a subset of representative cases, specifically: Mavic 2 Pro at 25 GHz in a quasi-monostatic configuration, Matrice 300 RTK at 25 GHz with $\theta_b = 20^\circ$, QR at 28 GHz with $\theta_b = 40^\circ$, and RA at 28 GHz with $\theta_b = 60^\circ$. The behavior of the measured RCS data at other frequencies and θ_b demonstrates consistent trends and similar fitting performance to the selected representative cases. To ensure completeness, the fitting parameters for all frequencies and θ_b are provided in tabular form for all test targets, facilitating a comprehensive understanding of the statistical characteristics across the different measurement configurations.

1) *RCS Distribution Modeling for UAV Test Cases:* The RCS distribution for the UAV test targets comprises two distinct platforms: the Mavic 2 Pro and the Matrice 300 RTK. Note that the RCS measurements were conducted while the UAVs were flying and rotating over the observation point. The rotation of the UAVs facilitated comprehensive RCS measurements, capturing the scattering profiles from all perspectives, including frontal and lateral views. Consequently, the measured RCS inherently encapsulates the orientation dependency of the UAV test targets, ensuring a detailed characterization of the RCS in the measured data.

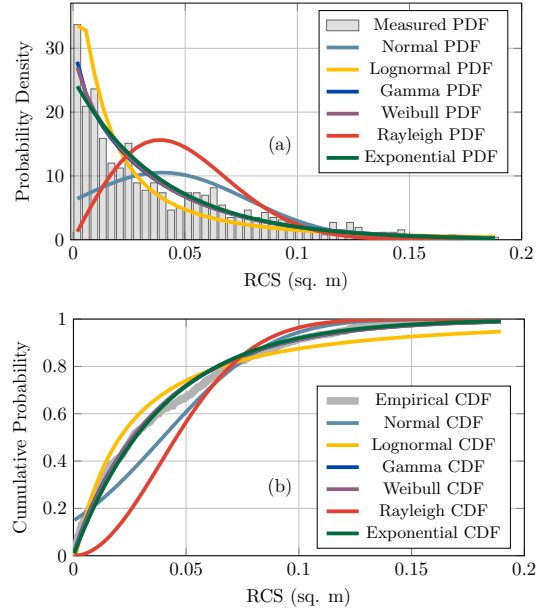


Fig. 6: RCS Distribution Modeling for Mavic 2 Pro at 25GHz for $\theta_b \approx 10^\circ$: (a) PDF Fitting, (b) CDF Fitting.

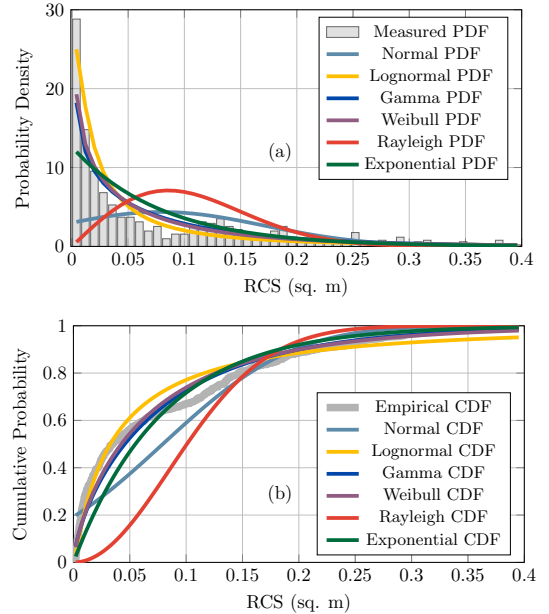


Fig. 7: RCS Distribution Modeling for Matrice 300 RTK at 25GHz for $\theta_b = 20^\circ$: (a) PDF Fitting, (b) CDF Fitting.

Fig. 6 illustrates the parametric distribution fitting to the measured RCS data at 25 GHz in a quasi-monostatic configuration for Mavic 2 Pro. Fig. 6(a) presents the PDF fitting, while Fig. 6(b) shows the corresponding CDF fitting between the measured data and the theoretical distributions. Table II provides a summary of the fitting results. From Fig. 6(a), we observe that the measured RCS data is positively skewed; thus, distributions such as lognormal, Weibull, exponential, and gamma align closely with the measured PDF, accurately capturing the skewness and tail characteristics. Furthermore, we can also observe that the backscatter reflections from the Mavic 2 Pro are generally weak. As detailed in Table II, the gamma distribution provides the best fit based on GoF metrics. Exponential, Weibull and lognormal distributions also

TABLE II: Parameters at 25 GHz for varying θ_b for Mavic.

25 GHz, $\theta_b \approx 10^\circ$			
Dist.	KS Stat ($\times 10^{-2}$)	MSE ($\times 10^{-3}$)	Parameters
Normal	15	6.7	$\mu = 0.04, \sigma = 0.038$
Lognormal	8.8	2.3	$\mu = -3.9, \sigma = 1.4$
Gamma	5	0.43	$A = 0.9, B = 0.044$
Weibull	5.2	0.52	$A = 0.039, B = 0.95$
Rayleigh	29	33	$B = 0.039$
Exponential	5.2	0.87	$\lambda = 0.04$
25 GHz, $\theta_b = 20^\circ$			
Normal	16	7.1	$\mu = 0.05, \sigma = 0.049$
Lognormal	13	7.5	$\mu = -3.90, \sigma = 1.67$
Gamma	13	4.4	$A = 0.66, B = 0.076$
Weibull	14	5.1	$A = 0.044, B = 0.77$
Rayleigh	33	35	$B = 0.05$
Exponential	20	9.2	$\lambda = 0.05$
25 GHz, $\theta_b = 40^\circ$			
Normal	18	11	$\mu = 0.046, \sigma = 0.051$
Lognormal	10	2.9	$\mu = -3.92, \sigma = 1.64$
Gamma	4.4	0.22	$A = 0.70, B = 0.066$
Weibull	4.2	0.32	$A = 0.041, B = 0.80$
Rayleigh	34	54	$B = 0.048$
Exponential	10	2.8	$\lambda = 0.046$
25 GHz, $\theta_b = 60^\circ$			
Normal	16	6.3	$\mu = 0.044, \sigma = 0.044$
Lognormal	13	4.4	$\mu = -3.96, \sigma = 1.64$
Gamma	8.1	1.6	$A = 0.71, B = 0.062$
Weibull	8.7	2	$A = 0.04, B = 0.81$
Rayleigh	32	35	$B = 0.044$
Exponential	13	4.3	$\lambda = 0.044$

demonstrate good fitting as they capture the skewed nature of the measured RCS data. However, the normal and Rayleigh distributions show significant deviations, failing to account for the measured RCS data's asymmetry. Similar conclusions can be drawn from the fitting of the empirical CDF and the measured RCS data CDF as shown in Fig. 6(b), where lognormal, Weibull, exponential, and gamma distributions demonstrate a strong agreement with the empirical CDF, reinforcing their suitability for modeling the observed RCS behavior.

Fig. 7 illustrates the parametric distribution fitting to the measured RCS data of the Matrice 300 RTK at 25GHz for $\theta_b = 20^\circ$. Note that the Matrice 300 RTK, with its larger dimensions compared to the Mavic 2 Pro, is expected to exhibit a higher RCS. The increase in RCS is attributed to its larger reflective surface area, which contributes to powerful backscatter. Additionally, the lithium-ion battery mounted at the rear of the Matrice 300 RTK introduces significant specular reflections, which are foreseen to dominate the scattering profile relative to other structural components of the UAV, leading to an increase in RCS.

The analysis of Fig. 7(a) and (b) reveals an observation that is consistent with that for the Mavic 2 Pro, i.e., the RCS distribution exhibits a positive skewness, characterized by a dominance of low-magnitude reflections and occasional high-magnitude specular reflections that contribute to higher RCS values. However, the specular reflections are notably more pronounced for the Matrice 300 RTK compared to the Mavic 2 Pro (cf. Fig. 6(a)). Statistical models, including the lognormal, Weibull, and gamma distributions, effectively capture the underlying characteristics of the RCS's PDF. As detailed in Table VI, the Weibull distribution best fits the

TABLE III: Parameters at 26 GHz for varying θ_b for Mavic.

26 GHz, $\theta_b \approx 10^\circ$			
Dist.	KS Stat ($\times 10^{-2}$)	MSE ($\times 10^{-3}$)	Parameters
Normal	14	6.3	$\mu = 0.024, \sigma = 0.014$
Lognormal	7.8	1.4	$\mu = -3.8, \sigma = 0.52$
Gamma	9.2	2.4	$A = 3.66, B = 0.0066$
Weibull	12	3	$A = 0.027, B = 1.86$
Rayleigh	11	4.2	$B = 0.019$
Exponential	32	20	$\lambda = 0.024$
26 GHz, $\theta_b = 20^\circ$			
Normal	12	4	$\mu = 0.036, \sigma = 0.031$
Lognormal	12	5.4	$\mu = -3.9, \sigma = 1.48$
Gamma	7	1	$A = 0.98, B = 0.036$
Weibull	6	0.83	$A = 0.036, B = 1.02$
Rayleigh	23	20	$B = 0.034$
Exponential	6.8	1	$\lambda = 0.036$
26 GHz, $\theta_b = 40^\circ$			
Normal	34	42	$\mu = 0.12, \sigma = 0.29$
Lognormal	5.4	1.1	$\mu = -3.9, \sigma = 2.2$
Gamma	15	6.8	$A = 0.35, B = 0.35$
Weibull	8.3	1.7	$A = 0.056, B = 0.4996$
Rayleigh	71	190	$B = 0.22$
Exponential	36	60	$\lambda = 0.12$
26 GHz, $\theta_b = 60^\circ$			
Normal	29	26	$\mu = 0.063, \sigma = 0.11$
Lognormal	3.1	0.2	$\mu = -3.95, \sigma = 1.71$
Gamma	9.4	2.8	$A = 0.52, B = 0.12$
Weibull	5.6	0.86	$A = 0.043, B = 0.64$
Rayleigh	57	130	$B = 0.093$
Exponential	23	21	$\lambda = 0.063$

TABLE IV: Parameters at 27 GHz for varying θ_b for Mavic.

27 GHz, $\theta_b \approx 10^\circ$			
Dist.	KS Stat ($\times 10^{-2}$)	MSE ($\times 10^{-3}$)	Parameters
Normal	22	15	$\mu = 0.067, \sigma = 0.088$
Lognormal	8.7	2.7	$\mu = -3.83, \sigma = 1.74$
Gamma	9.9	2.1	$A = 0.55, B = 0.12$
Weibull	9.4	1.8	$A = 0.05, B = 0.66$
Rayleigh	44	78	$B = 0.078$
Exponential	22	15	$\lambda = 0.067$
27 GHz, $\theta_b = 20^\circ$			
Normal	16	8.4	$\mu = 0.038, \sigma = 0.039$
Lognormal	12	4.3	$\mu = -3.9, \sigma = 1.46$
Gamma	4.5	4	$A = 0.89, B = 0.043$
Weibull	4.1	3.5	$A = 0.038, B = 0.94$
Rayleigh	30	37	$B = 0.039$
Exponential	3	0.21	$\lambda = 0.038$
27 GHz, $\theta_b = 40^\circ$			
Normal	18	8.3	$\mu = 0.053, \sigma = 0.06$
Lognormal	11	4	$\mu = -3.94, \sigma = 1.80$
Gamma	6.2	1.4	$A = 0.6, B = 0.087$
Weibull	7.6	1.9	$A = 0.044, B = 0.72$
Rayleigh	38	47	$B = 0.056$
Exponential	16	7.5	$\lambda = 0.053$
27 GHz, $\theta_b = 60^\circ$			
Normal	25	21	$\mu = 0.038, \sigma = 0.049$
Lognormal	9.3	3.3	$\mu = -3.97, \sigma = 1.17$
Gamma	15	8.2	$A = 0.82, B = 0.046$
Weibull	13	6	$A = 0.034, B = 0.84$
Rayleigh	50	91	$B = 0.044$
Exponential	19	12	$\lambda = 0.038$

measured data, followed closely by the gamma and lognormal distributions, which also display good alignment based on GoF evaluations. The empirical CDF further supports this observation in Fig. 7(b), where the Weibull, lognormal, and gamma distributions exhibit strong consistency with the em-

TABLE V: Parameters at 28 GHz for varying θ_b for Mavic.

28 GHz, $\theta_b \approx 10^\circ$			
Dist.	KS Stat ($\times 10^{-2}$)	MSE ($\times 10^{-3}$)	Parameters
Normal	19	11	$\mu = 0.027, \sigma = 0.023$
Lognormal	6	0.81	$\mu = -3.79, \sigma = 0.61$
Gamma	8.4	2.4	$A = 2.50, B = 0.011$
Weibull	13	3.8	$A = 0.031, B = 1.42$
Rayleigh	21	20	$B = 0.025$
Exponential	25	13	$\lambda = 0.027$
28 GHz, $\theta_b = 20^\circ$			
Normal	12	4.6	$\mu = 0.045, \sigma = 0.04$
Lognormal	15	8.6	$\mu = -3.81, \sigma = 1.77$
Gamma	8.6	1.8	$A = 0.80, B = 0.056$
Weibull	7.5	1.3	$A = 0.044, B = 0.92$
Rayleigh	23	22	$B = 0.043$
Exponential	6.2	8.4	$\lambda = 0.045$
28 GHz, $\theta_b = 40^\circ$			
Normal	25	21	$\mu = 0.027, \sigma = 0.029$
Lognormal	9.2	1.9	$\mu = -3.88, \sigma = 0.69$
Gamma	13	6.1	$A = 1.83, B = 0.015$
Weibull	18	7.3	$A = 0.029, B = 1.21$
Rayleigh	34	54	$B = 0.028$
Exponential	25	10	$\lambda = 0.027$
28 GHz, $\theta_b = 60^\circ$			
Normal	20	15	$\mu = 0.04, \sigma = 0.047$
Lognormal	4.5	0.57	$\mu = -3.91, \sigma = 1.24$
Gamma	8.5	2.4	$A = 0.84, B = 0.047$
Weibull	7.5	1.5	$A = 0.037, B = 0.87$
Rayleigh	41	69	$B = 0.043$
Exponential	12	4.9	$\lambda = 0.04$

pirical CDF, underscoring their suitability for modeling the observed RCS characteristics.

The fitting results for the measured RCS data of the Mavic 2 Pro to various parametric distributions are summarized in Tables II-V, encompassing different θ_b and operating frequencies. Similarly, the fitting results for the measured RCS data of the Matrice 300 RTK are detailed in Tables VI-IX for same θ_b and frequencies. For both UAVs, the KS statistics and MSE were computed for each distribution to evaluate the GoF. Based on the analysis presented in Tables II-V for the Mavic 2 Pro and Tables VI-IX for the Matrice 300 RTK, the following observations can be inferred

- 1) The Weibull, lognormal, and gamma distributions consistently provide the best fit. Specifically, the gamma distribution demonstrates superior performance in 12 out of the 32 representative cases, encompassing various θ_b and operating frequencies. In contrast, the lognormal and Weibull distributions achieve the best fit in 9 cases each. Exponential distribution is the best fit in 2 cases. However, the differences in the GoF metrics among these distributions are minimal in most representative cases. Thus, any of these three distributions can effectively model the RCS of the UAVs.
- 2) Considering the parameters of the best-fit distributions, it is observed that an increase in frequency for a given θ_b , marginally increases the RCS.
- 3) For both UAVs, the RCS decreases with an increase in the θ_b for all frequencies. The directional scattering characteristics, i.e., reduced contribution of the specular reflections, the material's and structural properties' angular dependency, etc. may explain the trends observed

TABLE VI: Parameters at 25 GHz for varying θ_b for Matrice.

25 GHz, $\theta_b \approx 10^\circ$			
Dist.	KS Stat ($\times 10^{-2}$)	MSE ($\times 10^{-3}$)	Parameters
Normal	19	11	$\mu = 0.063, \sigma = 0.072$
Lognormal	10	2.3	$\mu = -3.5, \sigma = 1.42$
Gamma	4.1	0.4	$A = 0.79, B = 0.079$
Weibull	4	0.4	$A = 0.058, B = 0.86$
Rayleigh	33	54	$B = 0.068$
Exponential	8.9	1.8	$\lambda = 0.063$
25 GHz, $\theta_b = 20^\circ$			
Normal	20	13	$\mu = 0.075, \sigma = 0.09$
Lognormal	10	2.2	$\mu = -3.54, \sigma = 1.59$
Gamma	8.7	2.6	$A = 0.63, B = 0.12$
Weibull	8.1	2.2	$A = 0.062, B = 0.73$
Rayleigh	44	64	$B = 0.083$
Exponential	19	12	$\lambda = 0.075$
25 GHz, $\theta_b = 40^\circ$			
Normal	19	12	$\mu = 0.054, \sigma = 0.063$
Lognormal	8.6	2.4	$\mu = -3.59, \sigma = 1.36$
Gamma	4.6	0.32	$A = 0.85, B = 0.063$
Weibull	4.2	0.29	$A = 0.051, B = 0.89$
Rayleigh	34	56	$B = 0.059$
Exponential	4.7	0.79	$\lambda = 0.054$
25 GHz, $\theta_b = 60^\circ$			
Normal	20	13	$\mu = 0.072, \sigma = 0.089$
Lognormal	8	1.7	$\mu = -3.62, \sigma = 1.70$
Gamma	4.6	0.57	$A = 0.61, B = 0.11$
Weibull	4.9	0.53	$A = 0.059, B = 0.72$
Rayleigh	41	67	$B = 0.081$
Exponential	15	8.5	$\lambda = 0.072$

in the RCS; however, it is difficult to quantify the relative contribution of each parameter.

- 4) Based on the following parameters of the best-fit distributions, it is evident that the RCS of the Matrice 300 RTK is higher compared to that of the Mavic 2 Pro. A primary contributing factor is the larger physical dimensions of the Matrice 300 RTK. Additionally, the placement of the lithium-ion battery at one end of the Matrice 300 RTK results in occasional strong specular reflections, which increases the RCS. While material properties may also influence the RCS, quantifying their specific impact remains challenging due to the complexity of their contribution to scattering behavior.

2) *RCS Distribution Modeling for Robotic Arm:* The analysis of the RA's RCS data at 28 GHz and $\theta_b = 60^\circ$ is shown in Fig. 8 which illustrates the fit of different parametric distributions to the measured RCS data. The PDF in Fig. 8(a) reveals that among the fitted statistical models, Weibull, Gamma, and lognormal distributions closely align with the PDF of the measured RCS data, effectively capturing the nature of backscatter from the RA. The best fit, however, is provided by Weibull distribution. The fitting results for different distributions are summarized in Table XIII. Models such as the Normal and Rayleigh distributions fail to adequately represent the measured RCS data, as they cannot take into account the impact of a high number of weak reflections and a low number of specular reflections while fitting the measured RCS data highlighting their limitations in modeling asymmetric distributions. The empirical CDF, as shown in Fig. 8 (b), further validates these findings.

The fitting results for the measured RCS data of the RA

TABLE VII: Parameters at 26 GHz for varying θ_b for Matrice.

26 GHz, $\theta_b \approx 10^\circ$			
Dist.	KS Stat ($\times 10^{-2}$)	MSE ($\times 10^{-3}$)	Parameters
Normal	19	11	$\mu = 0.066, \sigma = 0.074$
Lognormal	7.1	1.3	$\mu = -3.49, \sigma = 1.47$
Gamma	3.3	0.26	$A = 0.77, B = 0.085$
Weibull	2.2	1.3	$A = 0.06, B = 0.84$
Rayleigh	38	57	$B = 0.07$
Exponential	8.5	2.6	$\lambda = 0.066$
26 GHz, $\theta_b = 20^\circ$			
Normal	17	8.6	$\mu = 0.097, \sigma = 0.1$
Lognormal	15	7.5	$\mu = -3.53, \sigma = 2.26$
Gamma	7.6	1.6	$A = 0.52, B = 0.18$
Weibull	8.4	2.3	$A = 0.077, B = 0.65$
Rayleigh	34	46	$B = 0.1$
Exponential	15	5.7	$\lambda = 0.097$
26 GHz, $\theta_b = 40^\circ$			
Normal	17	7.2	$\mu = 0.08, \sigma = 0.085$
Lognormal	14	6.5	$\mu = -3.56, \sigma = 2$
Gamma	8.1	1.5	$A = 0.59, B = 0.13$
Weibull	8.9	2	$A = 0.06, B = 0.72$
Rayleigh	31	40	$B = 0.083$
Exponential	13	4.1	$\lambda = 0.08$
26 GHz, $\theta_b = 60^\circ$			
Normal	20	13	$\mu = 0.074, \sigma = 0.089$
Lognormal	8.6	2.3	$\mu = -3.59, \sigma = 1.7462$
Gamma	3.4	0.29	$A = 0.61, B = 0.12$
Weibull	4.3	0.34	$A = 0.061, B = 0.72$
Rayleigh	39	67	$B = 0.082$
Exponential	14	6.8	$\lambda = 0.074$

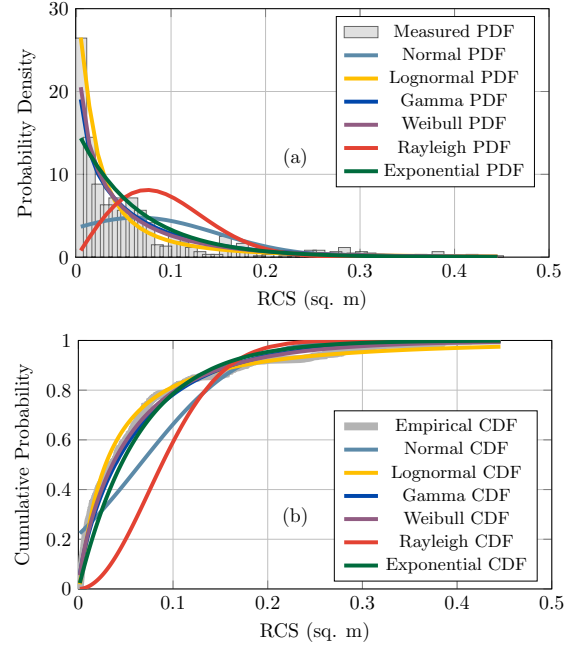
TABLE VIII: Parameters at 27 GHz for varying θ_b for Matrice.

27 GHz, $\theta_b \approx 10^\circ$			
Dist.	KS Stat ($\times 10^{-2}$)	MSE ($\times 10^{-3}$)	Parameters
Normal	16	7.2	$\mu = 0.092, \sigma = 0.093$
Lognormal	14	6	$\mu = -3.47, \sigma = 1.96$
Gamma	9.3	2.9	$A = 0.57, B = 0.16$
Weibull	10	3.7	$A = 0.075, B = 0.69$
Rayleigh	35	38	$B = 0.092$
Exponential	17	9.2	$\lambda = 0.092$
27 GHz, $\theta_b = 20^\circ$			
Normal	20	12	$\mu = 0.077, \sigma = 0.092$
Lognormal	7.8	1.4	$\mu = -3.49, \sigma = 1.63$
Gamma	5.7	0.78	$A = 0.64, B = 0.11$
Weibull	4.6	0.67	$A = 0.065, B = 0.74$
Rayleigh	41	63	$B = 0.085$
Exponential	15	7.7	$\lambda = 0.077$
27 GHz, $\theta_b = 40^\circ$			
Normal	22	18	$\mu = 0.057, \sigma = 0.071$
Lognormal	3.9	0.4	$\mu = -3.53, \sigma = 1.19$
Gamma	10	3.5	$A = 0.86, B = 0.065$
Weibull	8.6	2.2	$A = 0.053, B = 0.87$
Rayleigh	44	80	$B = 0.064$
Exponential	13	5.7	$\lambda = 0.057$
27 GHz, $\theta_b = 60^\circ$			
Normal	18	10	$\mu = 0.078, \sigma = 0.089$
Lognormal	10	4	$\mu = -3.58, \sigma = 1.87$
Gamma	5.2	0.5	$A = 0.59, B = 0.13$
Weibull	6.3	0.96	$A = 0.064, B = 0.71$
Rayleigh	37	54	$B = 0.084$
Exponential	14	6	$\lambda = 0.078$

to various parametric distributions are presented in Tables X-XIII, encompassing all θ_b and operating frequencies. The same GoF metrics employed for the UAVs are utilized to assess the accuracy of each distribution's fit. From the results summarized in Tables X-XIII, the following inferences can be

TABLE IX: Parameters at 28 GHz for varying θ_b for Matrice.

28 GHz, $\theta_b \approx 10^\circ$			
Dist.	KS Stat ($\times 10^{-2}$)	MSE ($\times 10^{-3}$)	Parameters
Normal	18	10	$\mu = 0.066, \sigma = 0.073$
Lognormal	8.2	1.6	$\mu = -3.49, \sigma = 1.48$
Gamma	4.7	0.41	$A = 0.76, B = 0.087$
Weibull	4.3	0.42	$A = 0.06, B = 0.83$
Rayleigh	35	50	$B = 0.069$
Exponential	10	3	$\lambda = 0.066$
28 GHz, $\theta_b = 20^\circ$			
Normal	20	13	$\mu = 0.081, \sigma = 0.097$
Lognormal	8.6	1.8	$\mu = -3.52, \sigma = 1.67$
Gamma	7.9	1.5	$A = 0.607, B = 0.13$
Weibull	7	1.3	$A = 0.065, B = 0.71$
Rayleigh	41	66	$B = 0.089$
Exponential	19	11	$\lambda = 0.081$
28 GHz, $\theta_b = 40^\circ$			
Normal	19	12	$\mu = 0.084, \sigma = 0.099$
Lognormal	8.5	2.3	$\mu = -3.56, \sigma = 1.84$
Gamma	5.2	0.69	$A = 0.57, B = 0.14$
Weibull	5.2	0.87	$A = 0.067, B = 0.69$
Rayleigh	41	63	$B = 0.092$
Exponential	17	10	$\lambda = 0.084$
28 GHz, $\theta_b = 60^\circ$			
Normal	19	11	$\mu = 0.083, \sigma = 0.095$
Lognormal	10	4.9	$\mu = -3.57, \sigma = 2.14$
Gamma	3.2	0.26	$A = 0.57, B = 0.14$
Weibull	3.9	0.43	$A = 0.068, B = 0.7$
Rayleigh	37	58	$B = 0.089$
Exponential	14	5.7	$\lambda = 0.083$

Fig. 8: RCS Distribution Modeling for RA at 28GHz for $\theta_b = 60^\circ$: (a) PDF Fitting, (b) CDF Fitting.

drawn:

- 1) Lognormal, Weibull, and gamma distributions demonstrate the best fit for the measured RCS data of the RA. Among these, gamma and Weibull distributions each perform optimally in 7 of the 16 representative cases, spanning various θ_b and operating frequencies. The lognormal distribution provides the best fit in 2 cases. Similar to the observations for UAVs, the differences

TABLE X: Parameters at 25 GHz for varying θ_b for RA.

25 GHz, $\theta_b \approx 10^\circ$			
Dist.	KS Stat ($\times 10^{-2}$)	MSE ($\times 10^{-3}$)	Parameters
Normal	20	13	$\mu = 0.085, \sigma = 0.098$
Lognormal	11	3.2	$\mu = -3.43, \sigma = 1.79$
Gamma	4.3	0.34	$A = 0.63, B = 0.13$
Weibull	4.5	0.45	$A = 0.072, B = 0.74$
Rayleigh	39	63	$B = 0.092$
Exponential	14	5	$\lambda = 0.085$
25 GHz, $\theta_b = 20^\circ$			
Normal	18	9.4	$\mu = 0.10, \sigma = 0.11$
Lognormal	11	4.7	$\mu = -3.48, \sigma = 2.23$
Gamma	8.4	1.1	$A = 0.52, B = 0.19$
Weibull	9.7	1.6	$A = 0.08, B = 0.65$
Rayleigh	39	50	$B = 0.1$
Exponential	18	9.5	$\lambda = 0.1$
25 GHz, $\theta_b = 40^\circ$			
Normal	11	3.3	$\mu = 0.04, \sigma = 0.03$
Lognormal	10	3.1	$\mu = -3.5, \sigma = 1.08$
Gamma	7.1	1.1	$A = 1.29, B = 0.03$
Weibull	6.3	1.1	$A = 0.049, B = 1.21$
Rayleigh	22	14	$B = 0.041$
Exponential	8.2	1.9	$\lambda = 0.046$
25 GHz, $\theta_b = 60^\circ$			
Normal	16	7.5	$\mu = 0.09, \sigma = 0.09$
Lognormal	15	9.5	$\mu = -3.52, \sigma = 2.35$
Gamma	8	1.9	$A = 0.55, B = 0.16$
Weibull	8.4	2	$A = 0.076, B = 0.69$
Rayleigh	32	40	$B = 0.093$
Exponential	11	3.5	$\lambda = 0.091$

in the GoF metrics among these three distributions are minimal in most cases.

- 2) The fitting parameters of the best-fit distributions reveal that an increase in θ_b leads to a reduction in the RCS at a fixed operating frequency, which can be attributed to the same factors previously discussed for UAVs.
- 3) It has been observed that the RCS reduces with an increase in frequency for a fixed θ_b , which is consistent with what has been observed for UAVs.
- 4) The RCS of RA is notably higher than that of the UAVs, where the RCS difference is attributed to its composition, which includes materials that significantly enhance backscatter. In contrast, UAVs predominantly consist of materials such as plastic and carbon fiber, which exhibit lower reflectivity, resulting in reduced RCS values.

3) *RCS Distribution Modeling for Quadruped Robot:* The fitting of the measured RCS data for a QR at 28 GHz and $\theta_b = 40^\circ$ is depicted in Fig. 9. The measured RCS data exhibits a positively skewed PDF, characterized by a predominance of weak reflections and a limited number of strong backscatter reflections from the target, which is anticipated because the continuous movement of the QR introduces orientation-dependent variations in the RCS. Consequently, strong reflections are observed when the robot's orientation favors specular backscatter, while weak reflections occur when the orientation reduces effective backscatter.

Fig. 9(a) indicates that the lognormal distribution provides the closest fit to the measured RCS data. Our findings are further corroborated by the GoF metrics summarized in Table XVII. The Weibull and Exponential distributions show mod-

TABLE XI: Parameters at 26 GHz for varying θ_b for RA.

26 GHz, $\theta_b \approx 10^\circ$			
Dist.	KS Stat ($\times 10^{-2}$)	MSE ($\times 10^{-3}$)	Parameters
Normal	20	13	$\mu = 0.08, \sigma = 0.09$
Lognormal	11	3.4	$\mu = -3.45, \sigma = 1.83$
Gamma	4.3	0.34	$A = 0.62, B = 0.13$
Weibull	4.4	0.46	$A = 0.07, B = 0.73$
Rayleigh	39	63	$B = 0.091$
Exponential	14	5.1	$\lambda = 0.084$
26 GHz, $\theta_b = 20^\circ$			
Normal	15	6.2	$\mu = 0.058, \sigma = 0.058$
Lognormal	10	3.1	$\mu = -3.49, \sigma = 1.41$
Gamma	5.3	0.51	$A = 0.88, B = 0.066$
Weibull	5.4	0.57	$A = 0.057, B = 0.93$
Rayleigh	30	33	$B = 0.058$
Exponential	5.6	0.76	$\lambda = 0.058$
26 GHz, $\theta_b = 40^\circ$			
Normal	21	15	$\mu = 0.08, \sigma = 0.1$
Lognormal	10	1.8	$\mu = -3.54, \sigma = 1.64$
Gamma	8.9	2.3	$A = 0.59, B = 0.13$
Weibull	7.5	1.8	$A = 0.064, B = 0.7$
Rayleigh	47	73	$B = 0.092$
Exponential	20	14	$\lambda = 0.08$
26 GHz, $\theta_b = 60^\circ$			
Normal	25	20	$\mu = 0.069, \sigma = 0.089$
Lognormal	5.1	0.62	$\mu = -3.55, \sigma = 1.47$
Gamma	11	3.8	$A = 0.68, B = 0.1$
Weibull	9.7	2.4	$A = 0.058, B = 0.76$
Rayleigh	48	91	$B = 0.08$
Exponential	20	12	$\lambda = 0.069$

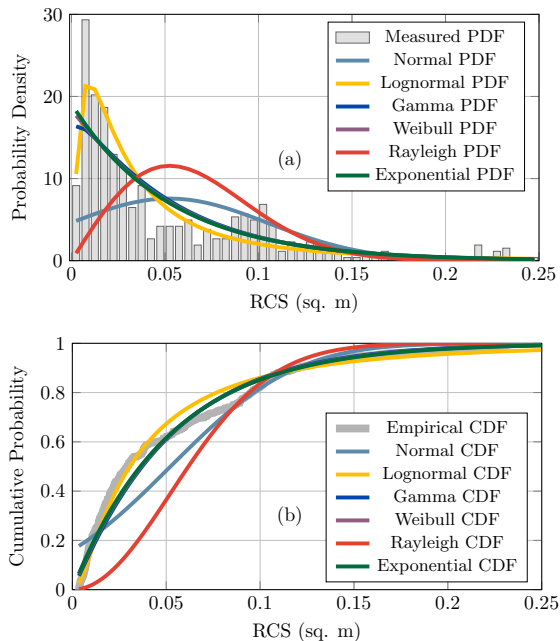
TABLE XII: Parameters at 27 GHz for varying θ_b for RA.

27 GHz, $\theta_b \approx 10^\circ$			
Dist.	KS Stat ($\times 10^{-2}$)	MSE ($\times 10^{-3}$)	Parameters
Normal	20	12	$\mu = 0.089, \sigma = 0.1$
Lognormal	8.5	2.6	$\mu = -3.48, \sigma = 1.82$
Gamma	6.9	0.96	$A = 0.5820, B = 0.15$
Weibull	7.1	1.1	$A = 0.072, B = 0.69$
Rayleigh	42	62	$B = 0.095$
Exponential	16	10	$\lambda = 0.089$
27 GHz, $\theta_b = 20^\circ$			
Normal	21	13	$\mu = 0.083, \sigma = 0.10$
Lognormal	9.2	2	$\mu = -3.48, \sigma = 1.75$
Gamma	4.3	0.32	$A = 0.61, B = 0.13$
Weibull	3.4	0.3	$A = 0.068, B = 0.72$
Rayleigh	40	69	$B = 0.093$
Exponential	14	6.8	$\lambda = 0.083$
27 GHz, $\theta_b = 40^\circ$			
Normal	13	7.4	$\mu = 0.032, \sigma = 0.015$
Lognormal	6.1	0.6	$\mu = -3.52, \sigma = 0.38$
Gamma	7.5	1.8	$A = 6.18, B = 0.0052$
Weibull	14	6	$A = 0.036, B = 2.17$
Rayleigh	16	7.1	$B = 0.025$
Exponential	37	37	$\lambda = 0.032$
27 GHz, $\theta_b = 60^\circ$			
Normal	21	14	$\mu = 0.074, \sigma = 0.089$
Lognormal	6.1	0.94	$\mu = -3.54, \sigma = 1.59$
Gamma	6.9	1.3	$A = 0.64, B = 0.11$
Weibull	6.1	0.89	$A = 0.062, B = 0.74$
Rayleigh	45	71	$B = 0.082$
Exponential	16	9.5	$\lambda = 0.074$

erate alignment. The empirical CDF in Fig. 9(b) also validates these results, demonstrating strong agreement between the empirical data and the fitted lognormal and Weibull distributions. The measured RCS data of the QR, fitted to various parametric distributions, is summarized in Tables XIV-XVII,

TABLE XIII: Parameters at 28 GHz for varying θ_b for RA.

28 GHz, $\theta_b \approx 10^\circ$			
Dist.	KS Stat ($\times 10^{-2}$)	MSE ($\times 10^{-3}$)	Parameters
Normal	15	7	$\mu = 0.069, \sigma = 0.069$
Lognormal	13	5	$\mu = -3.49, \sigma = 1.67$
Gamma	5.8	0.78	$A = 0.73, B = 0.094$
Weibull	5.8	0.99	$A = 0.063, B = 0.83$
Rayleigh	30	36	$B = 0.069$
Exponential	8.7	1.7	$\lambda = 0.069$
28 GHz, $\theta_b = 20^\circ$			
Normal	19	11	$\mu = 0.062, \sigma = 0.072$
Lognormal	8.5	1.7	$\mu = -3.52, \sigma = 1.39$
Gamma	6.3	0.68	$A = 0.78, B = 0.079$
Weibull	5.7	0.56	$A = 0.057, B = 0.84$
Rayleigh	35	55	$B = 0.067$
Exponential	11	3	$\lambda = 0.062$
28 GHz, $\theta_b = 40^\circ$			
Normal	17	8.8	$\mu = 0.09, \sigma = 0.095$
Lognormal	13	6	$\mu = -3.54, \sigma = 2.24$
Gamma	7.7	1.2	$A = 0.54, B = 0.16$
Weibull	8.7	1.7	$A = 0.07, B = 0.68$
Rayleigh	37	45	$B = 0.09$
Exponential	16	6.8	$\lambda = 0.09$
28 GHz, $\theta_b = 60^\circ$			
Normal	22	16	$\mu = 0.064, \sigma = 0.083$
Lognormal	7	1	$\mu = -3.55, \sigma = 1.40$
Gamma	6.5	1.3	$A = 0.73, B = 0.08$
Weibull	5.4	0.67	$A = 0.056, B = 0.79$
Rayleigh	41	78	$B = 0.074$
Exponential	13	5.9	$\lambda = 0.064$

Fig. 9: RCS Distribution Modeling for QR at 28GHz for $\theta_b = 40^\circ$: (a) PDF Fitting, (b) CDF Fitting.

covering all considered θ_b and operating frequencies. The GoF metrics evaluate each distribution's accuracy. The following conclusions can be drawn from the results:

- 1) Lognormal distribution provides the best fit with the measured RCS data in most of the representative cases. Among these, the lognormal distribution performs best in 7 out of 16 representative cases, transiting various θ_b and operating frequencies. The Weibull, gamma, and exponential distributions best fit in 4, 4, and 1 cases,

Distribution of Best-fit (KS) across targets

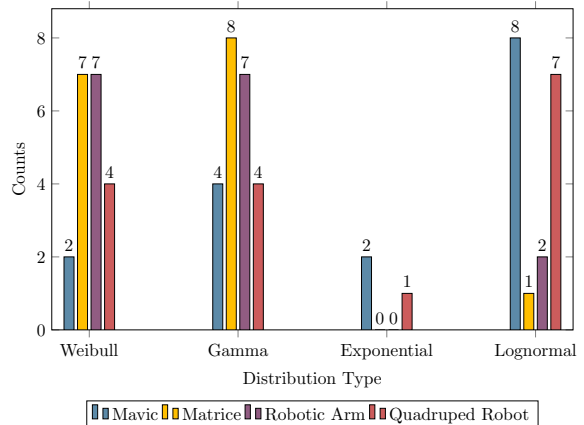


Fig. 10: Unified selected distributions over 25-28 GHz and all bistatic angles.

respectively. The differences in terms of GoF metrics between lognormal, Weibull and gamma distributions are minimal in most cases.

- 2) It is observed that the RCS decreases with an increase in the bistatic angle across all considered frequencies. Furthermore, the RCS slightly increases with an increase in the operating frequency for a given θ_b .

TABLE XIV: Parameters at 25 GHz for varying θ_b for QR.

25 GHz, $\theta_b \approx 10^\circ$			
Dist.	KS Stat ($\times 10^{-2}$)	MSE ($\times 10^{-3}$)	Parameters
Normal	18	10	$\mu = 0.072, \sigma = 0.077$
Lognormal	9.9	2.1	$\mu = -3.44, \sigma = 1.52$
Gamma	5.1	0.8	$A = 0.73, B = 0.099$
Weibull	5.7	0.87	$A = 0.065, B = 0.81$
Rayleigh	38	49	$B = 0.074$
Exponential	10	4.3	$\lambda = 0.07$
25 GHz, $\theta_b = 20^\circ$			
Normal	17	8.6	$\mu = 0.055, \sigma = 0.054$
Lognormal	11	2.6	$\mu = -3.48, \sigma = 1.17$
Gamma	9.3	2.7	$A = 0.98, B = 0.056$
Weibull	8.9	2.5	$A = 0.054, B = 0.98$
Rayleigh	35	39	$B = 0.054$
Exponential	9.6	2.8	$\lambda = 0.055$
25 GHz, $\theta_b = 40^\circ$			
Normal	17	11	$\mu = 0.053, \sigma = 0.054$
Lognormal	5.2	0.86	$\mu = -3.50, \sigma = 1.18$
Gamma	5.9	0.86	$A = 0.99, B = 0.054$
Weibull	5.8	0.69	$A = 0.053, B = 0.98$
Rayleigh	32	47	$B = 0.054$
Exponential	6	0.88	$\lambda = 0.053$
25 GHz, $\theta_b = 60^\circ$			
Normal	19	13	$\mu = 0.046, \sigma = 0.048$
Lognormal	4.4	0.5	$\mu = -3.52, \sigma = 0.98$
Gamma	7.1	1.4	$A = 1.22, B = 0.038$
Weibull	7.3	1.3	$A = 0.048, B = 1.07$
Rayleigh	30	46	$B = 0.047$
Exponential	8.3	1.1	$\lambda = 0.046$

4) *Unified RCS Distribution:* In Fig. 10, the best distribution is selected over all frequencies and θ_b to formulate a histogram of all 4 targets with their underlying RCS distribution, based on the findings in Tables II-XVII. We see that the lognormal distribution is the selected distribution for Mavic and QR, whereas the gamma distribution is the selected distribution for Matrice and RA. Interestingly, both distributions are special instances of the more general generalized Gamma

TABLE XV: Parameters at 26 GHz for varying θ_b for QR.

26 GHz, $\theta_b \approx 10^\circ$			
Dist.	KS Stat ($\times 10^{-2}$)	MSE ($\times 10^{-3}$)	Parameters
Normal	18	10	$\mu = 0.055, \sigma = 0.056$
Lognormal	9.9	2	$\mu = -3.44, \sigma = 1.10$
Gamma	11	2.1	$A = 1.04, B = 0.053$
Weibull	10	1.7	$A = 0.055, B = 0.99$
Rayleigh	33	44	$B = 0.056$
Exponential	10	1.7	$\lambda = 0.055$
26 GHz, $\theta_b = 20^\circ$			
Normal	15	6.2	$\mu = 0.058, \sigma = 0.055$
Lognormal	10	3	$\mu = -3.46, \sigma = 1.3$
Gamma	7.9	1.3	$A = 0.92, B = 0.063$
Weibull	8.2	1.5	$A = 0.057, B = 0.95$
Rayleigh	32	32	$B = 0.057$
Exponential	9.7	1.9	$\lambda = 0.058$
26 GHz, $\theta_b = 40^\circ$			
Normal	14	5.3	$\mu = 0.058, \sigma = 0.055$
Lognormal	11	3.8	$\mu = -3.5, \sigma = 1.4$
Gamma	6.6	0.97	$A = 0.87, B = 0.066$
Weibull	6.7	1.1	$A = 0.057, B = 0.94$
Rayleigh	28	28	$B = 0.057$
Exponential	6.4	1.3	$\lambda = 0.058$
26 GHz, $\theta_b = 60^\circ$			
Normal	20	14	$\mu = 0.052, \sigma = 0.056$
Lognormal	5.7	1.1	$\mu = -3.55, \sigma = 1.14$
Gamma	10	3.2	$A = 0.96, B = 0.054$
Weibull	8.6	2.4	$A = 0.05, B = 0.94$
Rayleigh	39	60	$B = 0.054$
Exponential	10	3.7	$\lambda = 0.052$

TABLE XVI: Parameters at 27 GHz for varying θ_b for QR.

27 GHz, $\theta_b \approx 10^\circ$			
Dist.	KS Stat ($\times 10^{-2}$)	MSE ($\times 10^{-3}$)	Parameters
Normal	16	7.1	$\mu = 0.062, \sigma = 0.062$
Lognormal	14	4.2	$\mu = -3.42, \sigma = 1.3$
Gamma	9.2	2.2	$A = 0.89, B = 0.069$
Weibull	9.1	2.3	$A = 0.06, B = 0.93$
Rayleigh	32	33	$B = 0.062$
Exponential	11	3	$\lambda = 0.062$
27 GHz, $\theta_b = 20^\circ$			
Normal	15	8.5	$\mu = 0.069, \sigma = 0.068$
Lognormal	11	2.9	$\mu = -3.45, \sigma = 1.53$
Gamma	7.9	1.3	$A = 0.75, B = 0.092$
Weibull	8.4	1.6	$A = 0.064, B = 0.84$
Rayleigh	33	40	$B = 0.069$
Exponential	14	4.1	$\lambda = 0.069$
27 GHz, $\theta_b = 40^\circ$			
Normal	14	5	$\mu = 0.056, \sigma = 0.052$
Lognormal	10	3.6	$\mu = -3.47, \sigma = 1.29$
Gamma	6.9	1.6	$A = 0.95, B = 0.059$
Weibull	7.1	1.7	$A = 0.056, B = 0.98$
Rayleigh	29	26	$B = 0.054$
Exponential	7.6	1.8	$\lambda = 0.056$
27 GHz, $\theta_b = 60^\circ$			
Normal	22	17	$\mu = 0.059, \sigma = 0.067$
Lognormal	10	3.8	$\mu = -3.49, \sigma = 1.16$
Gamma	15	7	$A = 0.88, B = 0.067$
Weibull	13	5.5	$A = 0.055, B = 0.88$
Rayleigh	45	72	$B = 0.063$
Exponential	18	9.6	$\lambda = 0.059$

distribution, whose PDF is

$$f(x; a, d, p) = \frac{p}{a^d \Gamma(d/p)} x^{d-1} e^{-(x/a)^p}, \quad x > 0, \quad (4)$$

where a, d, p denote the scale, shape, and power parameters and $\Gamma(\cdot)$ is the gamma function. When $p = 1$, we get the

TABLE XVII: Parameters at 28 GHz for varying θ_b for QR.

28 GHz, $\theta_b \approx 10^\circ$			
Dist.	KS Stat ($\times 10^{-2}$)	MSE ($\times 10^{-3}$)	Parameters
Normal	15	7	$\mu = 0.06, \sigma = 0.057$
Lognormal	8.8	2	$\mu = -3.4, \sigma = 1.22$
Gamma	6.7	1.2	$A = 0.97, B = 0.061$
Weibull	6.6	1.2	$A = 0.059, B = 0.98$
Rayleigh	32	34	$B = 0.058$
Exponential	7.2	1.4	$\lambda = 0.06$
28 GHz, $\theta_b = 20^\circ$			
Normal	18	9.9	$\mu = 0.056, \sigma = 0.053$
Lognormal	10	1.8	$\mu = -3.45, \sigma = 1.19$
Gamma	9.9	2.3	$A = 0.99, B = 0.056$
Weibull	9.9	2.2	$A = 0.056, B = 0.99$
Rayleigh	34	40	$B = 0.054$
Exponential	9.9	2.3	$\lambda = 0.056$
28 GHz, $\theta_b = 40^\circ$			
Normal	18	10	$\mu = 0.0523, \sigma = 0.052$
Lognormal	8.1	1.5	$\mu = -3.48, \sigma = 1.09$
Gamma	9.5	2.5	$A = 1.07, B = 0.048$
Weibull	8.6	2.1	$A = 0.052, B = 1.01$
Rayleigh	36	44	$B = 0.052$
Exponential	8.1	1.9	$\lambda = 0.052$
28 GHz, $\theta_b = 60^\circ$			
Normal	21	15	$\mu = 0.05, \sigma = 0.05$
Lognormal	5.7	0.9	$\mu = -3.56, \sigma = 1.09$
Gamma	9.8	3.4	$A = 1.0038, B = 0.05$
Weibull	8.6	2.5	$A = 0.049, B = 0.96$
Rayleigh	40	62	$B = 0.05$
Exponential	9.8	3.3	$\lambda = 0.05$

gamma distribution and when $p \rightarrow 0$, we get the lognormal distribution. p controls the skewness of the distribution. Notice that the Mavic is a lightweight and small drone, with rapid movements and surface material of plastic, magnesium, and carbon fiber. In addition, the QR, even though heavy, is a more dynamic target as compared to the RA. For Mavic and QR, lognormal appears to be the best-fit as reflections influenced by RCS can cover several orders of magnitude, whereas for more rigid bodies such as Matrice and RA the gamma distribution is the dominant distribution.

IV. FRAMEWORK FOR DETERMINISTIC RADAR CROSS SECTION EVALUATION

This section outlines a framework for the deterministic evaluation of the RCS.

A. Measurement Setup

The InH environment, shown in Figs. 1(c), is an indoor corridor nearby the KINESIS lab, which is 2.5 m in width, 28.5 m in length and 2.5 m in height. The target is a rectangular sheet of laminated wood with dimensions of 1.84 m \times 1.2 m. The NF distance for the target is calculated as $D = \frac{2S^2}{\lambda}$ [10], where D represents the NF distance, S is the largest dimension of the target (1.84 m in this case), and λ is the operating wavelength. For the given frequency range of 25 – 28 GHz, the selected target's NF distance lies approximately between 564 m and 632 m.

The central point of the line segment joining the Tx and the Rx is (0, 0). The Tx is positioned at $(-a, 0)$, while the Rx is located at $(a, 0)$, with $a = 0.7$ m. Target is placed at $(0, y)$, where y varies between 2 m and 10 m. The distance

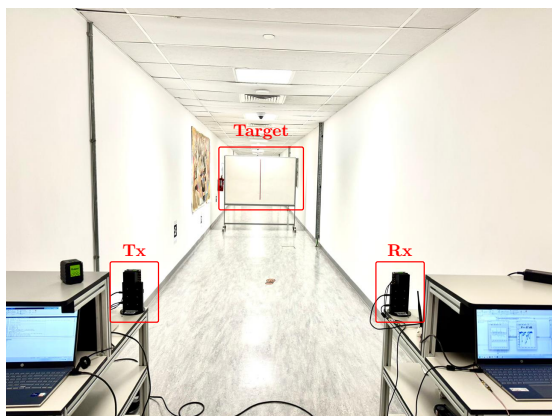


Fig. 11: The InH scenario for deterministic RCS evaluation.

between the Tx and the target, as well as the Rx and the target, is computed as $d = d_{\text{Tx,tar}} = d_{\text{Rx,tar}} = \sqrt{a^2 + y^2}$. Furthermore, the bistatic angle, which is a function of d and expressed in degrees for a target center located at y as:

$$\theta_b(d) = \left(1 - 2 \left(\frac{a}{d}\right)^2\right) \cdot \frac{180^\circ}{\pi}. \quad (5)$$

It may be noted that for different d considered in the measurements, $\theta_b(d)$ varies between approximately $38.37^\circ - 7.97^\circ$.

The same Tx and Rx RFICs are utilized for these measurements with an identical IF value as employed in the statistical RCS modeling. Additionally, identical ZC sequences are transmitted. However, at the Rx, PL is directly obtained. All the measurements are conducted for H-H polarizations considering LoS conditions. Moreover, the noise floor of our measurement setup is -72dB .

B. RCS Analysis

The PL equation for the bistatic system where $d = d_{\text{Tx,tar}} = d_{\text{Rx,tar}}$ is

$$\text{PL}_i(d, \lambda) = \alpha + 20n \log_{10}(d) - 10 \log_{10}(\sigma_i(d, \lambda)) + X_\sigma, \quad (6)$$

where α is the intercept acting as a bias, n is the PL exponent, $\sigma_i(d, \lambda)$ is the i th RCS model, and X_σ represents the shadowing effect. Similar to [6], the term in the single-way PL, namely $10n \log_{10}(d)$, is accounted for twice due to the two-way propagation, i.e. Tx towards target, then target towards Rx. The intercept term is an offset that is independent of d and λ and the RCS term depends on the material, size and shape of the target. Following [10], the NF RCS of the sheet depends on both distance and wavelength, because, in the NF region, the amount of energy reflected back towards the Rx varies with distance, as the signal may not fully illuminate the target at different NF distances. We explore multiple NF RCS models for the rectangular sheet, as

$$\begin{aligned} \sigma_1(d, \lambda) &= a_1 d^2 \cos^m(\theta_b(d)), \\ \sigma_2(d, \lambda) &= (a_1 d^2 + a_2 \lambda d^3) \cos^m(\theta_b(d)), \\ \sigma_3(d, \lambda) &= (a_1 d^2 + a_2 \lambda d^3 + a_3 \lambda^2 d^4) \cos^m(\theta_b(d)), \end{aligned} \quad (7)$$

where $\sigma_1(d, \lambda)$, $\sigma_2(d, \lambda)$, and $\sigma_3(d, \lambda)$ are the proposed bistatic RCS models for the rectangular sheet as functions of the distance d and the wavelength λ . a_1 , a_2 , and a_3 are fitting parameters that characterize the RCS based on the geometric properties of the target.

TABLE XVIII: Fitting parameters for deterministic RCS.

25 GHz									
Approx.	α	n	m	a_1	a_2	a_3	X_σ	MFE	
$\sigma_1(d, \lambda)$	51.41	1.85	-7.86	2.96	-	-	1.64	2.400	
$\sigma_2(d, \lambda)$	51.66	1.84	-8.13	2.91	1.25	-	1.63	2.377	
$\sigma_3(d, \lambda)$	51.82	1.83	-8.26	2.90	1.25	0.03	1.63	2.370	
26 GHz									
$\sigma_1(d, \lambda)$	44.21	1.90	-6.1	2.94	-	-	0.72	1.146	
$\sigma_2(d, \lambda)$	43.80	1.92	-6.02	2.90	1.25	-	0.72	1.144	
$\sigma_3(d, \lambda)$	43.65	1.92	-6.02	2.80	1.25	0.03	0.72	1.144	
27 GHz									
$\sigma_1(d, \lambda)$	43.78	1.95	-7.19	2.99	-	-	2.09	1.813	
$\sigma_2(d, \lambda)$	44.17	1.97	-7.04	3.50	1.01	-	2.03	1.791	
$\sigma_3(d, \lambda)$	43.99	1.98	-6.91	3.50	1.01	0.02	2.02	1.767	
28 GHz									
$\sigma_1(d, \lambda)$	46.80	1.85	-6.56	3.02	-	-	1.04	1.597	
$\sigma_2(d, \lambda)$	47.73	1.85	-6.68	3.25	1.01	-	1.04	1.582	
$\sigma_3(d, \lambda)$	47.56	1.85	-6.69	3.50	1.01	0.02	1.04	1.583	

To justify equation (6), we plot in Fig. 12 (a)-(d) the PL as function of distance, which as observed does not follow a linear growth pattern but instead reaches a plateau as d increases. This PL plateau is a characteristic of the NF regime, arising from the non-linear behavior of the NF RCS of the target. This trend remains consistent across the 25 – 28 GHz frequency range. Additionally, the fitted model corresponding to $\sigma_3(d, \lambda)$ demonstrates the lowest mean fitting error MFE among all the considered RCS models (see Table XVIII).

Since we have used only one rectangular sheet for our measurement, we cannot characterize the dependence of a_1 , a_2 , and a_3 on the area of the sheet. $\cos^m(\theta_b(d))$ captures the angular dependence of the bistatic RCS, where $\theta_b(d)$ is the bistatic angle as a function of distance d , and m is an angular exponent. d^2 , λd^3 , and $\lambda^2 d^4$ represent the terms that account for the NF scattering behavior of the rectangular sheet at different orders of distance and wavelength.

To evaluate the GoF, MFE is evaluated for each RCS model, where MFE in percentage is defined as

$$\text{MFE} = \frac{1}{N} \sum_{j=1}^N \left| \frac{\text{PL}_{\text{meas},j} - \text{PL}_{i,j}}{\text{PL}_{\text{meas},j}} \right| \times 100\% \quad (8)$$

where N is the total number of data points, $\text{PL}_{\text{meas},j}$ is the measured PL for the j -th data point, $\text{PL}_{i,j}$ is the i th modeled PL for the j -th data point. The primary distinction among the various PL models lies in the selection of the RCS model employed. Table XVIII presents the results of the fitting process for the different PL models across various frequencies. X_σ is evaluated as $\sqrt{\frac{1}{N} \sum_{j=1}^N (x_j - \mu)^2}$, where x_j represents the difference between the measured values and the fitted curve values, and μ denotes the average value of x_j . Furthermore, the fitted models based on the measured data are depicted in Fig. 12 (a)-(d) for the operating frequencies ranging from 25 – 28 GHz. To facilitate interpretation, the PL values are inverted by multiplying them by -1 in Fig. 12 (a)-(d), effectively representing the negative of the PL.

Table XVIII presents the fitting parameters for deterministic RCS models ($\sigma_1(d, \lambda)$, $\sigma_2(d, \lambda)$, and $\sigma_3(d, \lambda)$) across operating frequencies of 25 GHz, 26 GHz, 27 GHz, and 28 GHz. The intercept, α and PL exponent, n , show minor variations across frequencies and models, with α decreasing slightly as frequency increases (e.g., from 51.41 at 25 GHz to 47.56 at

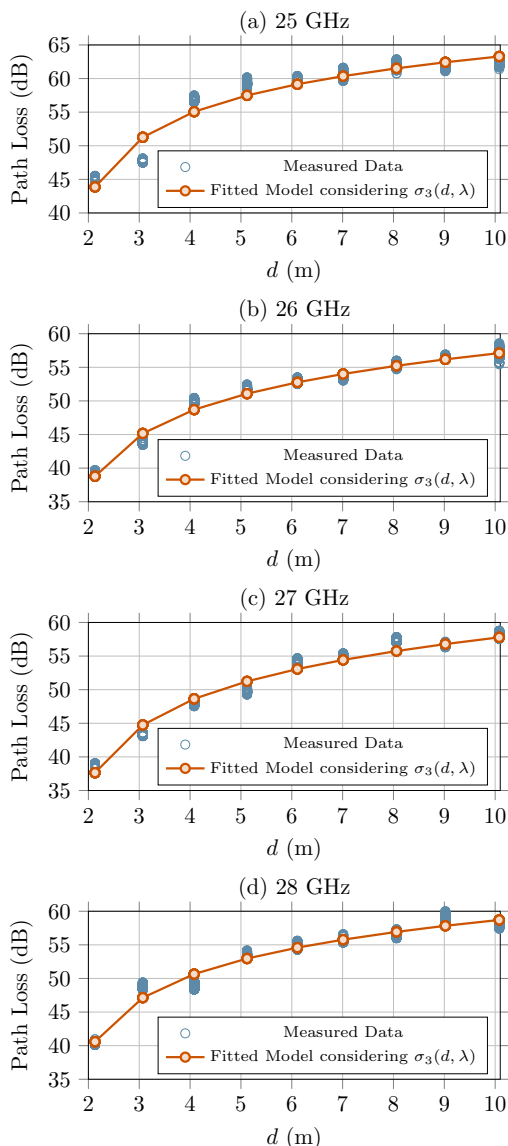


Fig. 12: Measured PL and model curve fitting in the NF.

28 GHz) and n remains consistent, ranging from 1.83 to 1.98. The angular exponent, m , varies across frequencies, ranging from -8.26 at 25 GHz for $\sigma_3(d, \lambda)$ to -6.69 at 28 GHz for $\sigma_3(d, \lambda)$, indicating its sensitivity to frequency. The RCS model parameters, a_1 , a_2 , and a_3 are consistent within each frequency and model. The small values of the parameters a_2 and a_3 indicate their minor contributions towards the deterministic RCS. However, it is again highlighted that a_2 and a_3 also depend on the area of the rectangular sheet. The change in the area of the sheet would certainly change the values of a_2 and a_3 . The a_2 and a_3 parameters are expected to be higher for rectangular sheets with smaller areas. Among the models, $\sigma_3(d, \lambda)$ generally provides the lowest MFE, demonstrating better fitting performance. The MFE values decrease with increasing frequency, indicating improved fitting accuracy at higher frequencies. Overall, $\sigma_3(d, \lambda)$ is the most accurate model across all frequencies due to its inclusion of higher-order terms and consistently lower MFE values.

V. CONCLUSIONS

This study comprehensively characterizes the RCS of typical targets in InF and InH environments using statistical and deterministic modeling approaches. The statistical analysis involved fitting measured RCS data from test targets such as UAVs, RA, and QR to parametric distributions. The statistical analysis is performed for monostatic configuration as well as three different bistatic configurations for operating frequencies of 25–28 GHz. Weibull, lognormal, and gamma distributions, all of which are right-skewed distributions, were identified as optimal based on GoF metrics, effectively capturing the statistical variations in RCS induced by target geometry, material composition, dynamic operational conditions, etc. Furthermore, it has been observed that the RCS decreases with an increase in the bistatic angle. In the deterministic analysis, the bistatic RCS of a rectangular sheet of laminated wood was modeled by leveraging PL measurements across frequencies from 25 GHz to 28 GHz under NF conditions. Proposed RCS models, parameterized by bistatic angle and the distance between the Tx, Rx, and the target, were evaluated, and the best-fitting models were identified based on the MFE. The results indicate that RCS strongly depends on the bistatic angle and target distance, emphasizing the dependence of angular and spatial variability inherent in bistatic scattering on the RCS, which further highlights the critical role of RCS modeling in channel modeling for ISAC. Future work may focus on extending these models to other frequencies and environments.

REFERENCES

- [1] Ojas Kanhere, Sanjay Goyal, Mihaela Beluri, and Theodore S. Rappaport. Target Localization using Bistatic and Multistatic Radar with 5G NR Waveform. In *2021 IEEE 93rd Vehicular Technology Conference (VTC2021-Spring)*, pages 1–7, 2021.
- [2] Z. Wei, J. Jia, Y. Niu, L. Wang, H. Wu, H. Yang, and Z. Feng. Integrated Sensing and Communication Channel Modeling: A Survey. *IEEE Internet of Things Journal*, 2024.
- [3] Nadav Levanon. Radar principles. *New York*, 1988.
- [4] D. K. et al. Cheng. *Field and wave electromagnetics*. Pearson Education India, 1989.
- [5] B. H. Borden and M. L. Mumford. A statistical glint/radar cross section target model. *IEEE Transactions on Aerospace and Electronic Systems*, (5):781–785, 1983.
- [6] S.Y. Seidel, T.S. Rappaport, S. Jain, M.L. Lord, and R. Singh. Path loss, scattering and multipath delay statistics in four European cities for digital cellular and microcellular radiotelephone. *IEEE Transactions on Vehicular Technology*, 40(4):721–730, 1991.
- [7] Shihao Ju, Syed Hashim Ali Shah, Muhammad Affan Javed, Jun Li, Girish Palteru, Jyotish Robin, Yunchou Xing, Ojas Kanhere, and Theodore S. Rappaport. Scattering Mechanisms and Modeling for Terahertz Wireless Communications. In *ICC 2019 - 2019 IEEE International Conference on Communications (ICC)*, pages 1–7, 2019.
- [8] 3rd Generation Partnership Project (3GPP). Summary #3 on ISAC channel modelling. Discussion/Decision Document R1-2408100, 3GPP TSG RAN WG1, Hefei, China, October 2024. TSG RAN WG1 #118bis, Agenda item 9.7.2. Source: Moderator (Xiaomi).
- [9] D. Shakya, M. Ying, T. S. Rappaport, P. Ma, I. Al-Wazani, Y. Wu, Y. Wang, D. Calin, H. Poddar, A. Bazzi, M. Chafii, Y. Xing, and A. Ghosh. Urban Outdoor Propagation Measurements and Channel Models at 6.75 GHz FR1(C) and 16.95 GHz FR3 Upper Mid-band Spectrum for 5G and 6G. In *IEEE International Conference on Communications (ICC)*, pages 1–6, Montreal, Canada, June 2025. accepted.
- [10] P. Pouliguen, J. F. Damiens, R. Hemon, and J. Saillard. RCS computation in near field. In *DAYS on DIFFRACTION 2006*, pages 252–265, 2006.